remote sensing

MDPI

Technical Note

A New Type of Red-Green-Blue Composite and Its Application in Tropical Cyclone Center Positioning

Liren Chen [1], Xiaoyong Zhuge [2,*], Xiaodong Tang [1], Jinjie Song [2] and Yuan Wang [1]

[1] Key Laboratory of Mesoscale Severe Weather for Ministry of Education, School of Atmospheric Sciences, Nanjing University, Nanjing 210044, China; mg20280003@smail.nju.edu.cn (L.C.); xdtang@nju.edu.cn (X.T.); yuanasm@nju.edu.cn (Y.W.)
[2] Nanjing Joint Institute for Atmospheric Sciences, Nanjing 210041, China; songjj@cma.gov.cn
* Correspondence: zhugexy@cma.gov.cn

Abstract: Weak tropical cyclone (TC) center positioning is difficult work in operational forecasting. In the present study, a TC-red-green-blue (TC-RGB) composite was designed by using satellite multi-channel observations (reflectance, brightness temperature, and brightness temperature differences). Compared with single channel images, TC-RGB composites can clearly show the exposed low-level circulation (LLC) of weak TCs under large vertical wind shear. Based on the guidelines of TC-RGB composites for TC center positioning, we repositioned 83 western North Pacific (WNP) TC cases during 2017–2019. Then, the comparisons of TC center positions were made between the TC-RGB composite and the Regional Specialized Meteorological Centre-Tokyo (RSMC-Tokyo), the Joint Typhoon Warning Center (JTWC) and the China Meteorological Administration-Shanghai Typhoon Institute (CMA-STI). Via case analysis of TC Kalmaegi (2019), it was found that the best-track data from the RSMC-Tokyo, JTWC and CMA-STI would have over 100 km biases at the early stage of TC life history. Taking all the 83 TC cases into account, the results show that the average center position biases and standard deviations for weak TCs under small vertical wind shear in the daytime are 5 km larger than those under large vertical wind shear at nighttime. When considering the 83 TC cases with clear LLC centers, the difference of these two biases is 10 km. The average biases are mostly above 20 km in the areas south of 18° N and north of 36° N over the WNP. Conversely, in the areas between 18° N and 36° N over the WNP, they are mostly below 20 km.

Keywords: satellite application; RGB composite; tropical cyclones; center positioning

check for updates

Citation: Chen, L.; Zhuge, X.; Tang, X.; Song, J.; Wang, Y. A New Type of Red-Green-Blue Composite and Its Application in Tropical Cyclone Center Positioning. *Remote Sens.* **2022**, *14*, 539. https://doi.org/10.3390/rs14030539

Academic Editor: Xiaofeng Yang

Received: 18 December 2021
Accepted: 21 January 2022
Published: 23 January 2022

Publisher's Note: MDPI stays neutral with regard to jurisdictional claims in published maps and institutional affiliations.

Copyright: © 2022 by the authors. Licensee MDPI, Basel, Switzerland. This article is an open access article distributed under the terms and conditions of the Creative Commons Attribution (CC BY) license (https://creativecommons.org/licenses/by/4.0/).

1. Introduction

A tropical cyclone (TC) is a strong vortex system with a warm core originating from tropical or subtropical warm and humid ocean surfaces [1]. Coastal countries are devastatingly impacted by disasters brought about by TCs, such as strong winds, rainstorms and resulting floods and landslides [2]. Continuous TC monitoring and forecasting is an important part of operations for coastal national meteorological sectors [3,4]. Three key elements of a TC include its center position, intensity, and scale [5]. Among them, the TC center is defined as the low-level circulation (LLC) center or depression center in the mean sea-level pressure field [6]. TC center positioning is the basis for accurately analyzing and predicting TC intensity and scale [7–10]. Moreover, the accurate data of a TC center can be beneficial for initial multiphysics in model simulations and machine learning [11].

Current observational platforms for TCs mainly include aircraft, shore-based radars, and meteorological satellites. Aircraft detect the wind field near the TC center through dropwindsondes and a stepped frequency microwave radiometer to determine the TC center and structure [12,13]. Although this method is relatively accurate, it can only be used in offshore regions and possesses obvious shortcomings in terms of continuous observation. Shore-based radar can determine the TC center via the method of spiral line fitting on

echo images or by detecting the radial velocity field [14,15]. However, limited by their detection range (the maximum detection range of radial velocity is 230 km) and the effect of the earth's curvature, they are powerless for TCs prior to landfall [16]. Multispectral imagers carried by geostationary satellites can provide continuous images at visible (VIS) and infrared (IR) wavelengths. As a deep convective system, cold targets (i.e., upper-level TC clouds) are easily distinguished from sea background on IR images. In the past three decades, numerous IR-based algorithms for objective TC center positioning have been developed, such as the Dvorak Technique (DT) and Automated Rotational Center Hurricane Eye Retrieval [17–19]. These TC center positioning algorithms all assume upper- and lower-level circulation centers are consistent, and the LLC center is inferred through the distribution of the upper-level cloud system of the TC. Therefore, they are mainly effective when TC eye or spiral rain bands are obvious [20]. Under large vertical wind shear, the upper-level cloud system deviates obviously from the LLC and sometimes even exposes the LLC center. Due to the small temperature difference between low clouds and the sea surface, even if the LLC center is exposed, it is still not easy to find using IR images alone. Inversely, on VIS images, it is possible to highlight the LLC center (without high cloud cover). However, traditional VIS observations require suitable illumination conditions and cannot be used under low illumination conditions, such as at nighttime or in dawn/dusk hours [21].

Regarding the issue of weak TC center positioning under large vertical wind shear without VIS, microwave or low-light observational instruments on board polar-orbiting satellites are used. Passive microwave imagers and active microwave scatterometers both estimate the emissivity and roughness characteristics of the sea surface through measured radiances, which are determined by the sea surface wind speed and direction [22]. A low center of the wind field can be considered the LLC center [23,24]. However, a majority of microwave observations have non-negligible drawbacks, such as their coarse spatial resolution (25–50 km under sub-satellite points) and vulnerability to heavy rainfall. As a new tool for TC monitoring and forecasting in recent years, space-borne synthetic aperture radar (SAR) is capable of measuring sea surface winds with high spatial resolution (tens of meters) under almost all weather conditions [25]. The main limitation of SAR is its sporadic availability (an explanation will be given later). At the same time, the VIS IR Imaging Radiometer Suite onboard the United States new-generation polar-orbiting meteorological satellites has a highly sensitive, low-light channel called the Day Night Band (DNB) [26]. With a spatial resolution of 0.5 km, DNB can acquire moonlight and starlight reflection data under low illumination conditions, such as nighttime and dawn/dusk hours [21,27]. However, limited by the signal intensity of the light source, low-cloud monitoring by DNB is currently only effective under the conditions between a semilunar and full moon [28]. Additionally, another major shortcoming of the polar-orbiting satellite instrument is its low temporal resolution. Especially in tropical regions, continuous TC center positioning cannot be achieved due to usually just one or two observations a day [29].

Red-green-blue (RGB) composites, widely used in cloud microphysics in the past decade, solve problems in which a single channel has difficulty distinguishing between different targets [30]. Hawkins et al. [31] used RGB composites via a combination of DNB (VIS observations in daytime and low-light observations at nighttime) and IR channels to reveal that the centers of upper and lower levels have 100 km biases under large vertical wind shear. However, when the moonlight conditions are insufficient at nighttime, this method cannot be used. In the present study, a new TC-RGB composite was designed, which is available for all-day TC center positioning. This improvement is especially beneficial to the TCs with clear LLC centers. On this basis, the characteristics of center position biases between the TC-RGB-based method and the three agencies under different vertical wind shear conditions, intensity categories and geographical locations are analyzed.

2. Materials and Methods

2.1. Data

2.1.1. Best-Track Datasets

There are three agencies in the western North Pacific (WNP) region that provide data on TC tracks—namely, the Regional Specialized Meteorological Centre-Tokyo (RSMC-Tokyo), the Joint Typhoon Warning Center (JTWC) and the China Meteorological Administration-Shanghai Typhoon Institute (CMA-STI). The three best-track datasets have their own characteristics [32]. However, compared to other two best-track datasets, the JTWC dataset uses more data sources for its analyses [33]. For this paper, we selected the common part of the three datasets during 2017–2019, which consists of 83 TC cases. Not considering the differences in TC intensity categories of the three agencies, we considered the JTWC intensity categories as representative. These categories are: tropical depression (TD); tropical storm (TS); category 1–5 (C1–C5) on the Saffir–Simpson Hurricane Scale [34]; and extratropical systems (EX).

2.1.2. Vertical Wind Shear from Reanalysis Data

Reanalysis data are used in calculating the vertical wind shear for analyzing the characteristics of TC center position biases under different wind shear conditions. In this study, the United States National Centers for Environmental Prediction (NCEP) final (FNL) data [35] with 0.25° resolution at 6 h intervals were selected. They are available from July 2015.

According to DeMaria et al. [36], the environmental vertical wind shear of a TC can be defined as the difference between the average wind vector at 850 hPa and 200 hPa within the range of 200–800 km from the TC center. Here, the 850 hPa and 200 hPa wind field data are from the NCEP FNL reanalysis data. Later, the vertical wind shear is divided into large and small quantities according to a 20 knot (kt; 1 kt = 0.51 m s^{-1}) threshold.

2.1.3. Himawari-8 Observations

The Japanese geostationary meteorological satellite Himawari-8 was launched in October 2014 and became operational in July 2015. The sub-satellite point is located at 140.7° E. The Advanced Himawari Imager (AHI), as the main payload of Himawari-8, has 16 channels, including 3 VIS channels, 3 near-IR channels, and 10 IR channels [37]. Data from these channels can be used to estimate the top height, optical thickness, and other characteristics of clouds [38,39]. The spatial resolution of the AHI VIS channels (0.5 km under the sub-satellite point) is higher than that of IR channels (2 km under the sub-satellite point). For this paper, observations of all channels were resampled at a resolution of 2 km when using the TC-RGB composites. In addition, the original temporal resolution of the AHI is 10 min, but images are only used at half-hourly intervals. Correspondingly, the best-track datasets and vertical wind shear data, which have a resolution of once every 6 h, were also linearly interpolated every 30 min.

2.2. Design of TC-RGB Composites

Hawkins et al. [31] used an RGB composite with DNB observations modulating the red and green components and IR observations modulating the blue component, which is only effective when there is sunshine during the day or enough moonlight at night. However, the TC-RGB composites designed in this paper can be applied to TC center positioning throughout the day. For simplicity, it is divided into a day (night) mode according to the solar zenith angle less (greater) than 87° [40].

The day mode is similar to the method in Hawkins et al. [31]. Specifically, the reflectance of the AHI 0.4-μm VIS channel ($A_{0.4}$) modulates the red and green components. When $A_{0.4}$ is between 0 and 1, it linearly corresponds to 0–100% in the red and green components. When $A_{0.4}$ is less than 0 or more than 1, the two components are set to 0 and 100%, respectively. The specific linear transformation is illustrated in Figure 1a. The brightness temperature of the AHI 10.4-μm IR channel ($T_{10.4}$) inversely modulates the

blue component within the range of 203–323 K. If the value of $T_{10.4}$ is more than 323 K or less than 203 K, the blue component is set to 0 or 100%, respectively. The inversely linear transformation is illustrated in Figure 1b. $A_{0.4}$ and $T_{10.4}$ reflect the cloud optical thickness and cloud-top height, respectively. Cirrus, deep convective clouds, and low clouds are three common cloud types in TCs. Cirrus is thinner, with very low $A_{0.4}$, so it appears blue. Deep convective clouds have high cloud tops and large optical thicknesses, so all three components are large, appearing white. Low clouds have large $A_{0.4}$ values and low cloud tops, so they appear yellow. For land and sea, their $A_{0.4}$ ($T_{10.4}$) values are less (greater), thus appearing dark blue or dark gray. The typical physical values and colors of these targets are summarized in Table 1.

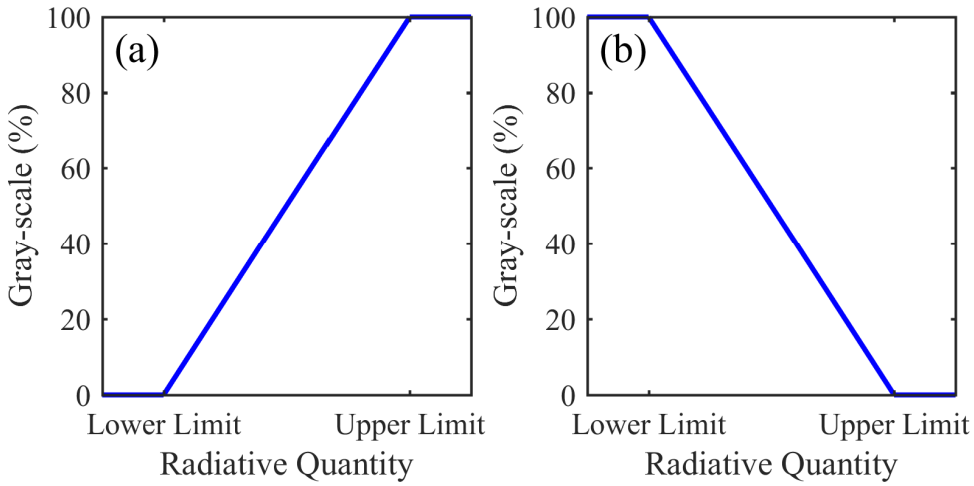


Figure 1. Illustrations of (**a**) normally and (**b**) inversely linear transformations from radiative quantity to gray-scale.

Table 1. Typical physical values (reflectance, brightness temperature or brightness temperature differ-ences) and colors for five objects in tropical cyclone (TC) red-green-blue (RGB) composites in day and night modes. The red-, green- or blue-color marked characters mean they are served as the red, green or blue component of RGB composites, respectively. First (last) values in parentheses are the lower (upper) limits for a normally or inversely linear map from radiative quantities to gray-scale.

Day Mode		$A_{0.4}$ (0, 1)	$A_{0.4}$ (0, 1)	$T_{10.4}$ (203 K, 323 K)	Color
Sea		0.08	0.08	295 K	
Land		0.21	0.21	300 K	
Cirrus		0.3	0.3	260 K	
Deep Cb		0.96	0.96	200 K	
Low cloud		0.86	0.86	290 K	
Night Mode		$T_{12.3–10.4}$ (−4 K, 2 K)	$T_{10.4–3.9}$ (−5 K, 5 K)	$T_{10.4}$ (203 K, 323 K)	**Color**
Sea	Summer	−3.5 K	−1.1 K	295 K	
	Winter	−2.7 K	0.1 K	288 K	
Land	Summer	−1.2 K	0.8 K	292 K	
	Winter	0 K	0.9 K	270 K	
Cirrus		−4.5 K	−11.5 K	255 K	
Deep Cb		0.7 K	−8.5 K	205 K	
Low cloud		−2.1 K	3.5 K	280 K	

To solve the problem of there being no VIS channel data at night, the night-mode TC-RGB composites proposed in this study use the brightness temperature difference. Specifically, the difference between $T_{10.4}$ and the AHI 12.3-μm IR brightness temperature ($T_{12.3–10.4}$) modulates the red component, ranging from −4 K to 2 K; the difference between the AHI 3.9-μm channel brightness temperature ($T_{3.9}$) and $T_{10.4}$ ($T_{10.4–3.9}$) modulates the

green component, ranging from −5 K to 5 K. The red and green components are set to 0 and 100%, as the value of $T_{12.3–10.4}$ or $T_{10.4–3.9}$ exceeds the lower and upper limits, based on the linear transformation illustrated in Figure 1a. The blue component is consistent with the day mode. $T_{12.3–10.4}$ mainly characterizes the optical thickness of clouds [41]. The $T_{12.3–10.4}$ of thin clouds (e.g., cirrus) is obviously negative, whereas for thick clouds, it is positive. $T_{10.4–3.9}$ reflects the difference in cloud emissivity at different wavelengths. The 3.9-μm emissivity of stratus clouds is lower than the 10.4-μm emissivity [42], which is significantly different from other clouds. Finally, in night-mode TC-RGB composites, cirrus appears blue, while low clouds appear bright green, and deep convective clouds appear dark violet (Table 1). Note that when $T_{3.9}$ is lower than 220 K, the signal-to-noise ratio is relatively small [43], resulting in unstable values of $T_{10.4–3.9}$. Thus, the "purply red" deep convective cloud often has light-cyan "spots". Due to seasonal variations in $T_{12.3–10.4}$, the sea shows dark green (green) in summer (winter), while land appears olive-drab (sandy brown) in summer (winter). Typical physical values and colors of these targets are also summarized in Table 1.

Figure 2 shows three examples of TC-RGB composites. Low clouds in yellow (bright green) are significantly different from the background and other clouds in daytime (at nighttime). Cirrus clouds appear blue throughout the day. Same clouds with similar colors in day and night modes ensure the consistency in applying and understanding the TC-RGB composites.

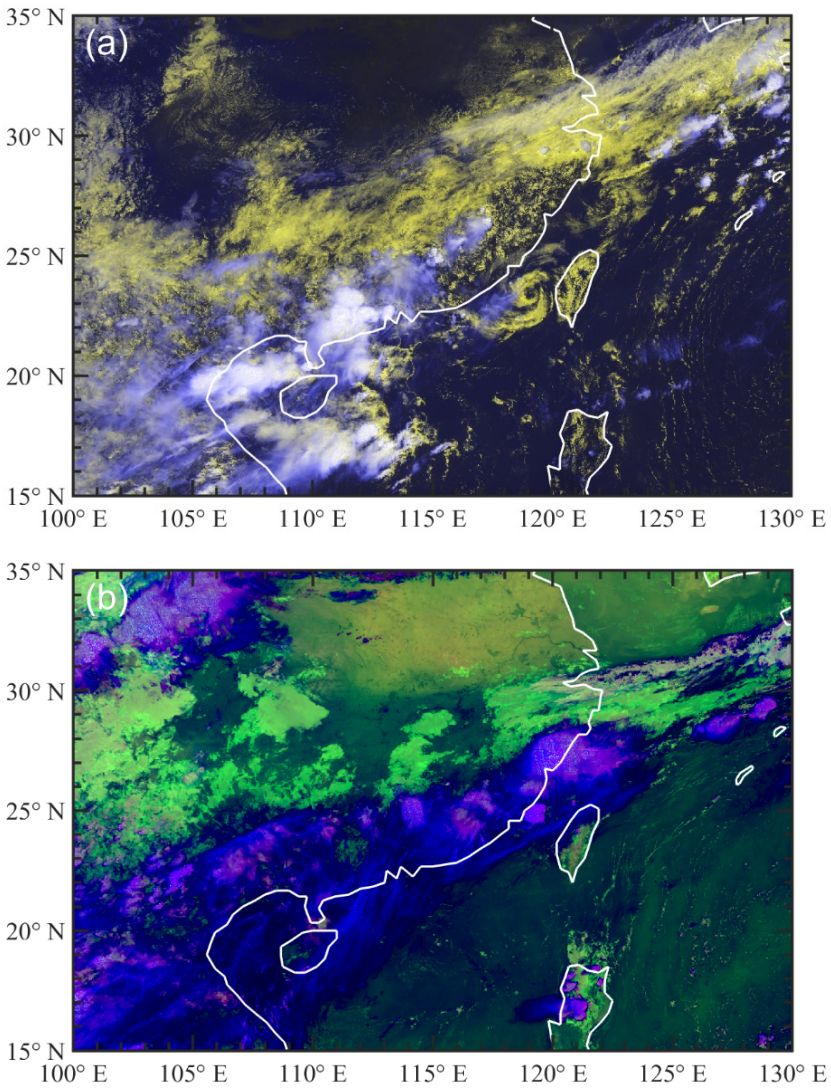


Figure 2. *Cont.*

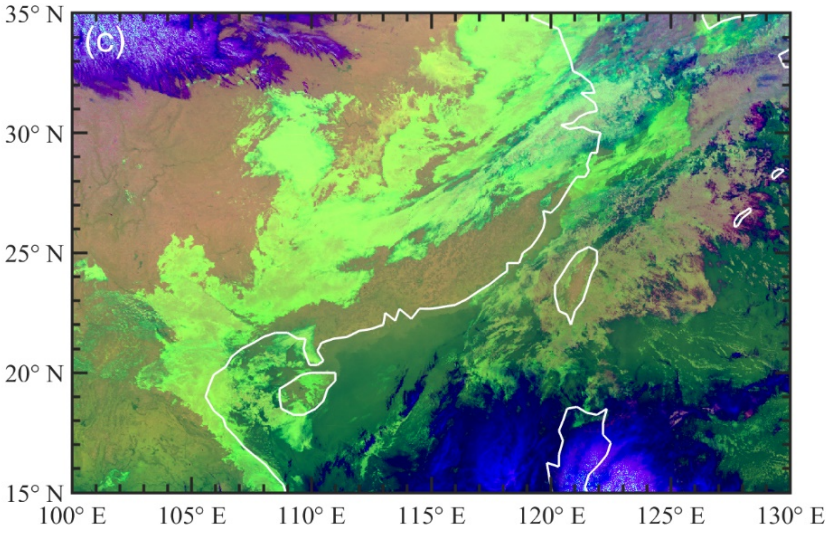


Figure 2. Examples of day- or night-mode TC-RGB composites by using Advanced Himawari Imager (AHI) observations at (**a**) 0400 UTC and (**b**) 1600 UTC on 7 September 2017, as well as (**c**) 1600 UTC on 16 January 2018.

2.3. Application of TC-RGB Composites in TC Center Positioning

2.3.1. Guidelines for Using TC-RGB Composites in TC Center Positioning

As shown in Figure 3, TCs with a certain intensity can be divided into two types: with and without an eye. For TCs with an eye, if the TC eye has a regular shape (e.g., circle, ellipse) and no cloud in the eye region, the center is located at the highest brightness temperature. If the TC eye has a regular shape but obvious low cloud in the eye region, the TC center is set at its geometric center. If the shape of the TC eye is not regular, the rotational center is set as the TC center by analyzing the three consecutive TC-RGB composites at the nearest time intervals.

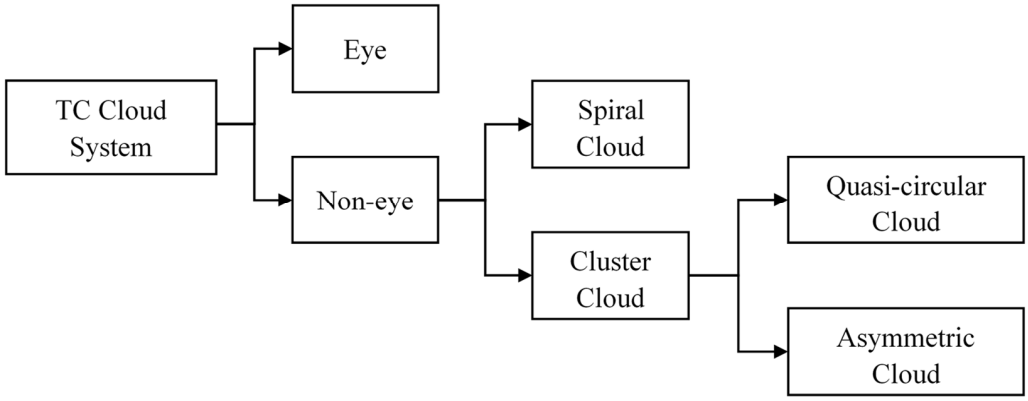


Figure 3. Classification of TC cloud systems for TC center positioning.

A non-eye TC cloud system can also be divided into two types according to its shape and the characteristics of the outside spiral cloud band, namely a spiral or cluster TC cloud system. A spiral TC cloud system is characterized by obvious spiral cloud bands around the TC. In contrast, a cluster TC cloud system appears as a central dense overcast (CDO) or central cold cover (CCC) on the image. Furthermore, according to its geometric shape, it can be divided into a quasi-circular or asymmetric TC cloud system. Figure 4 shows three examples of applying non-eye TC center positioning. According to the DT [44], the TC with spiral cloud bands is positioned by fitting of the spiral lines. Willoughby found that

these spiral cloud bands have the shape of logarithmic spirals [45]. The polar equations of logarithmic spirals are

$$r = ae^{b\theta}, \quad (1)$$

where a and b are quasi-constants. The parameter a represents the tightness of the logarithmic spiral line, while the parameter b characterizes the angle between the tangent of any point on the logarithmic spiral and the radius from the center to the point. Generally speaking, a (b) varies from 20 (0.16) to 35 (0.19) according to the intensity of the TC [46]. In Figure 4a, when choosing the parameters for the two major spiral cloud bands, TC center is positioned at the intersection point. The quasi-circular cloud TC is simply positioned at the geometric center (Figure 4b). In the asymmetrically distributed CDO (CCC), due to the vertical wind shear, the center positioning can be divided into two scenes by the degrees of exposure for the LLC. Similar to the rule in DT, for the TC without an exposed LLC, the center is generally located on the steeper side of the edge of the cold cloud area. Thus, in Figure 4c, the TC center is determined at that place as mentioned. For the TC with an exposed LLC, the exposed LLC appears yellow (in daytime) or bright green (in nighttime) through low clouds, distinguished from the background and other clouds. The spiral center of low clouds is identified as TC center. Because this part is the most important content for TC-RGB composite in TC center positioning, more details, including two typical examples will be given in Section 2.3.2 alone.

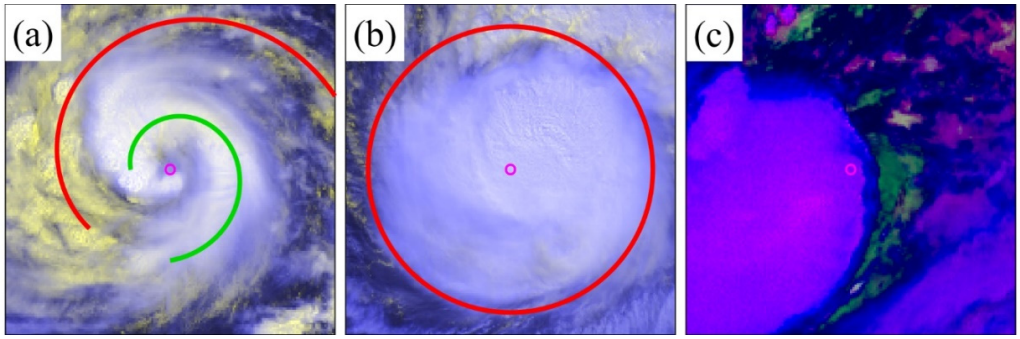


Figure 4. Examples of TC center positioning for TCs with (**a**) spiral cloud, (**b**) quasi-circular cloud and (**c**) asymmetric cloud. The TC-RGB-based centers are indicated by the magenta circles.

Finally, within the entire TC life cycle, the TC center positions should be as continuous as possible to avoid large jumps. In the animation of TC-RGB composites taking the TC-RGB-based center as the origin of coordinates, the TC should be only seen rotating without obvious jitter.

2.3.2. Typical Examples

Figure 5 shows two examples of the application of TC-RGB composites in TC center positioning. TC Jongdari (2018) at 1500 UTC on 30 July and TC Faxai (2018) at 0400 UTC on 3 September were at the TD and TS level, respectively. On their $T_{10.4}$ images (Figure 5a,d), convective clouds are on the east side, without an obvious spiral center. In Figure 5b (Figure 5e), due to the difference in emissivity (reflectance), the low cloud and background differ markedly in the $T_{10.4–3.9}$ image at nighttime ($A_{0.4}$ image in the daytime). By further using the TC-RGB composites, we can easily distinguish the low clouds from background and high clouds (Figure 5c,f). In Figure 5c, low clouds appear bright green, separated from the upper-level system. Thus, the center of TC Jongdari is set at the LLC center (indicated by magenta circle). The TC centers from the three best-track datasets were set at low clouds, 28–44 km northeast of the TC-RGB-based center. In Figure 5f, the exposed LLC shows as yellow. The TC centers from JTWC and CMA-STI are generally consistent with the TC-RGB-based center, with biases of less than 16 km. However, the TC center from RSMC-Tokyo is approximately 46 km east of the TC-RGB-based center. TC-RGB composites reveal the biases of best-track datasets in TC center positioning.

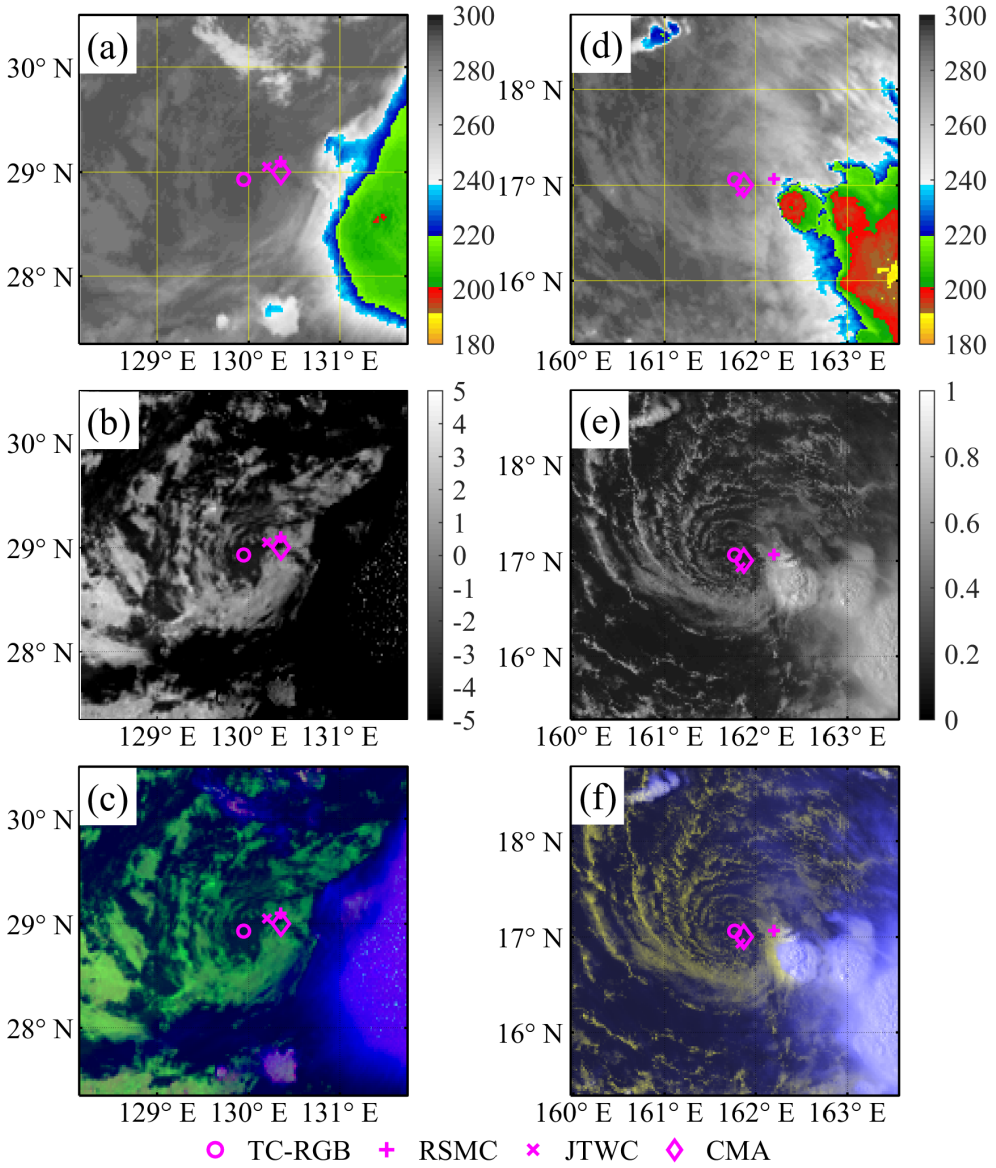


Figure 5. Images of (**a**) $T_{10.4}$ (unit: K), (**b**) $T_{10.4–3.9}$ (unit: K), and (**c**) TC-RGB in night mode for TC Jongdari (2018) observed at 1500 UTC on 30 July 2018, as well as images of (**d**) $T_{10.4}$ (unit: K), (**e**) $A_{0.4}$ (unitless), and (**f**) TC-RGB in day mode for TC Faxai (2018) observed at 0400 UTC on 3 September 2018. TC center positions from the three best-track datasets and the TC-RGB-based centers are indicated by magenta markers.

3. Results

In this section, we reveal the characteristics of center position biases and the standard deviations between the TC-RGB-based method and the best-track data from RSMC-Tokyo, JTWC and CMA-STI by using 83 TC cases in 2017–2019. The definition for the center position bias (x; unit: km) is

$$x = 6371 \cdot \sqrt{(\varnothing - \varnothing_0)^2 \cos^2 \theta_0 + (\theta - \theta_0)^2}, \quad (2)$$

where $\varnothing$ is the longitude (in radians) of the TC center position from any one of the three agencies and $\varnothing_0$ is the longitude (in radians) of the TC center position from the TC-RGB

method. Similarly, θ and θ_0 represent the latitude. Furthermore, the definition for the standard deviation (s; unit: km) of center position biases is

$$s = \sqrt{\frac{1}{n}\sum_{i=1}^{n}(x_i - \bar{x})^2}, \quad (3)$$

where $\bar{x}$ is the average center position bias and n is the number of the cases.

3.1. Case Analysis

Figure 6a shows the tracks of TC Kalmaegi (2019) from the three best-track datasets and the TC-RGB-based method. Three inset TC-RGB composites are used to prove the rationality of the TC-RGB-based track. On 13 November, Kalmaegi was at the TD level, with the exposed LLC center under relatively large vertical wind shear (approximately 17 kt). In the two TC-RGB composites, the TC-RGB-based centers are all set at the LLC center. However, the TC centers from the three best-track datasets differ greatly, especially those from CMA-STI. On 17 November, Kalmaegi reached the TS level, with a CCC in the upper level under small vertical wind shear (approximately 5 kt). However, the LLC center is faintly visible through gaps in upper-level clouds. The centers from JTWC and RSMC-Tokyo are consistent with the TC-RGB-based center, but the center from CMA-STI has a westward bias. Figure 6b illustrates track biases between the TC-RGB-based method and the three best-track datasets. The track biases of the three agencies are mostly less than 50 km but sometimes more than 100 km. When TC Kalmaegi is at the TD level, the track biases are relatively large. Around 14 July, under large vertical wind shear, the track bias between the TC-RGB-based method and CMA-STI (JTWC) can reach 250 (150) km. Conversely, when Kalmaegi reaches the TS or C1–C2 level, the track biases are generally below 50 km.

3.2. Overall Performances

For this paper, 83 TCs that occurred in the WNP from 2017 to 2019 were repositioned using TC-RGB composites. The average center position biases (standard deviations) between the TC-RGB-based method and best-track datasets from RSMC-Tokyo, JTWC and CMA-STI were calculated, and they are 14.338 km, 13.631 km and 17.097 km (13.581 km, 12.774 km and 15.459 km), respectively. Figure 7 shows the average center position biases and sample sizes of the three agencies under different vertical wind shear in daytime (left panel) or at nighttime (right panel). Due to the small number of TC samples at the EX level, we do not discuss these any further. In terms of TC intensity categories, as they become stronger, the average center position biases decrease from 25 km to 5 km. As shown in Figure 7, the average position biases of TCs under small vertical wind shear are not as large as those under large vertical wind shear. Due to large vertical wind shear, upper- and lower-level systems have greater separation, causing exposed LLC centers, which favors the use of TC-RGB composites. At present, agencies use VIS and IR images for TC center positioning in the daytime, which is the same as day-mode TC-RGB composites to some extent. However, they use IR images alone at nighttime. Thus, comparing the average position bias during daytime and nighttime, especially when a TC is weak (e.g., at the TD level), the average center position biases at nighttime are approximately 5 km larger than those in the daytime. Overall, weak TCs under small vertical wind shear at nighttime have relatively large average center position biases and standard deviations.

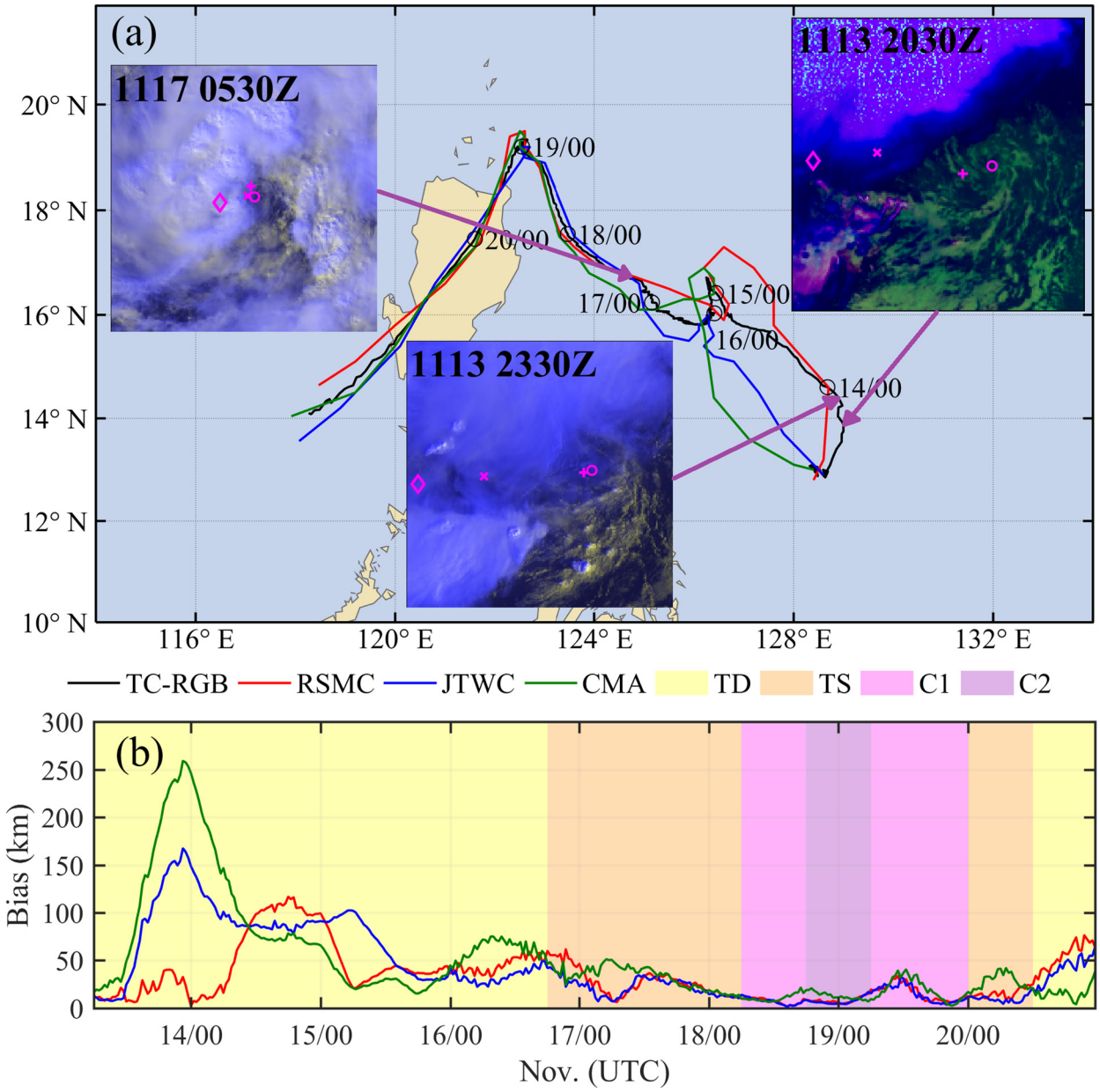


Figure 6. (**a**) Tracks of TC Kalmaegi (2019) from the three best-track datasets and the TC-RGB-based method. Purple lines link inset figures of TC-RGB composites to the approximate TC locations on the track. TC center positions from the three agencies and TC-RGB-based method are indicated by magenta markers (+: Regional Specialized Meteorological Centre-Tokyo (RSMC-Tokyo); ×: Joint Typhoon Warning Center (JTWC); ♢: China Meteorological Administration-Shanghai Typhoon Institute (CMA-STI); o: TC-RGB). (**b**) The bias of center positions between the TC-RGB-based method and each of the three best-track datasets for TC Kalmaegi (2019). The color shading indicates intensity categories.

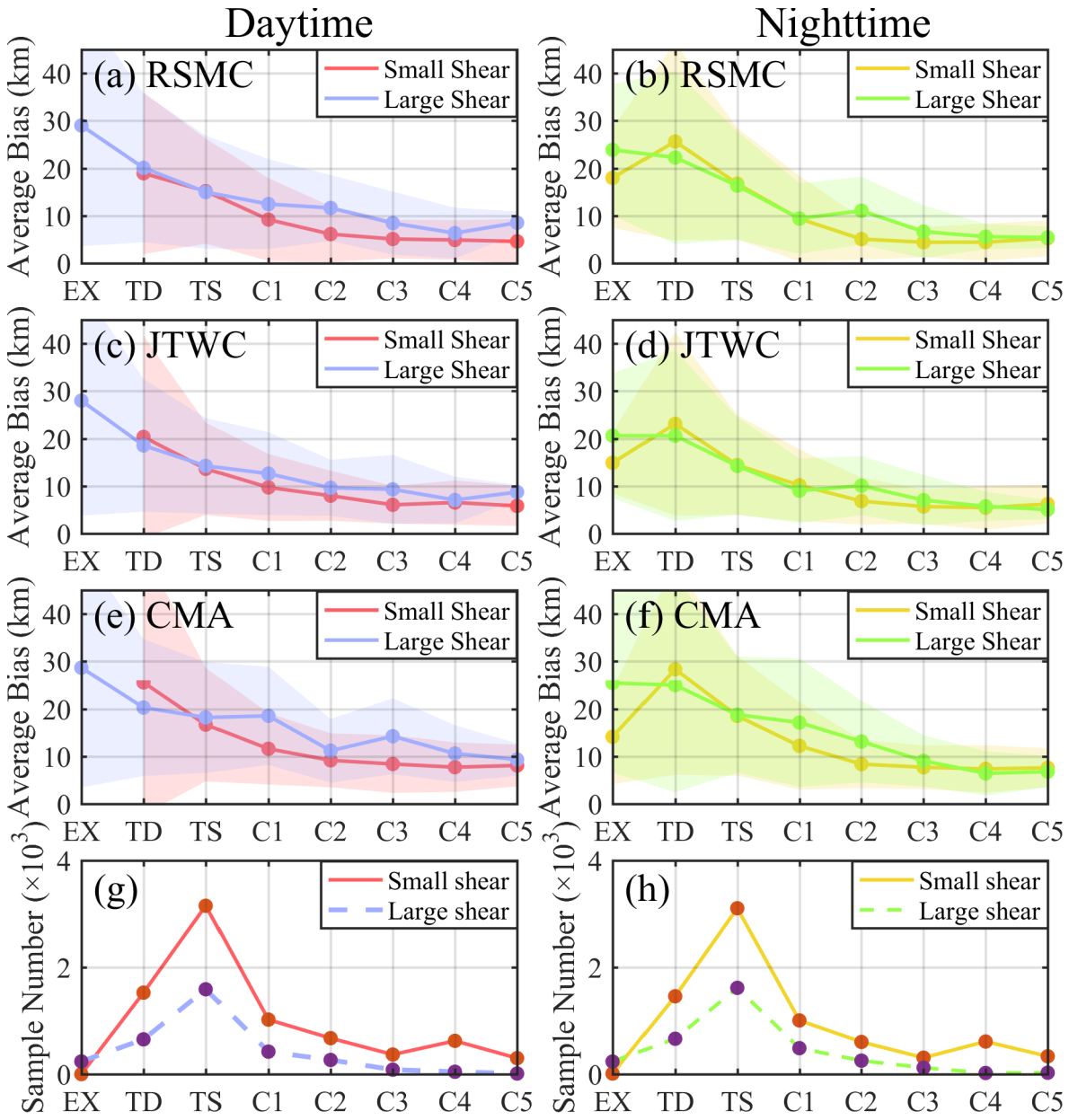


Figure 7. Average biases of the TC center positions between the TC-RGB-based method and the best-track datasets from (**a**,**b**) RSMC-Tokyo, (**c**,**d**) JTWC and (**e**,**f**) CMA-STI, along with (**g**,**h**) sample sizes, for 83 TC cases during 2017–2019 in each intensity category, with shading indicating the standard deviation. Comparisons were conducted for TCs under large/small vertical shear during daytime (left panel) as well as nighttime (right panel).

Furthermore, if only TC cases with clear LLC centers are selected (Figure 8), the difference in the average position biases between daytime and nighttime will be more significant. The biases at nighttime are approximately 10 km larger than those in the daytime, especially when the TC is weak.

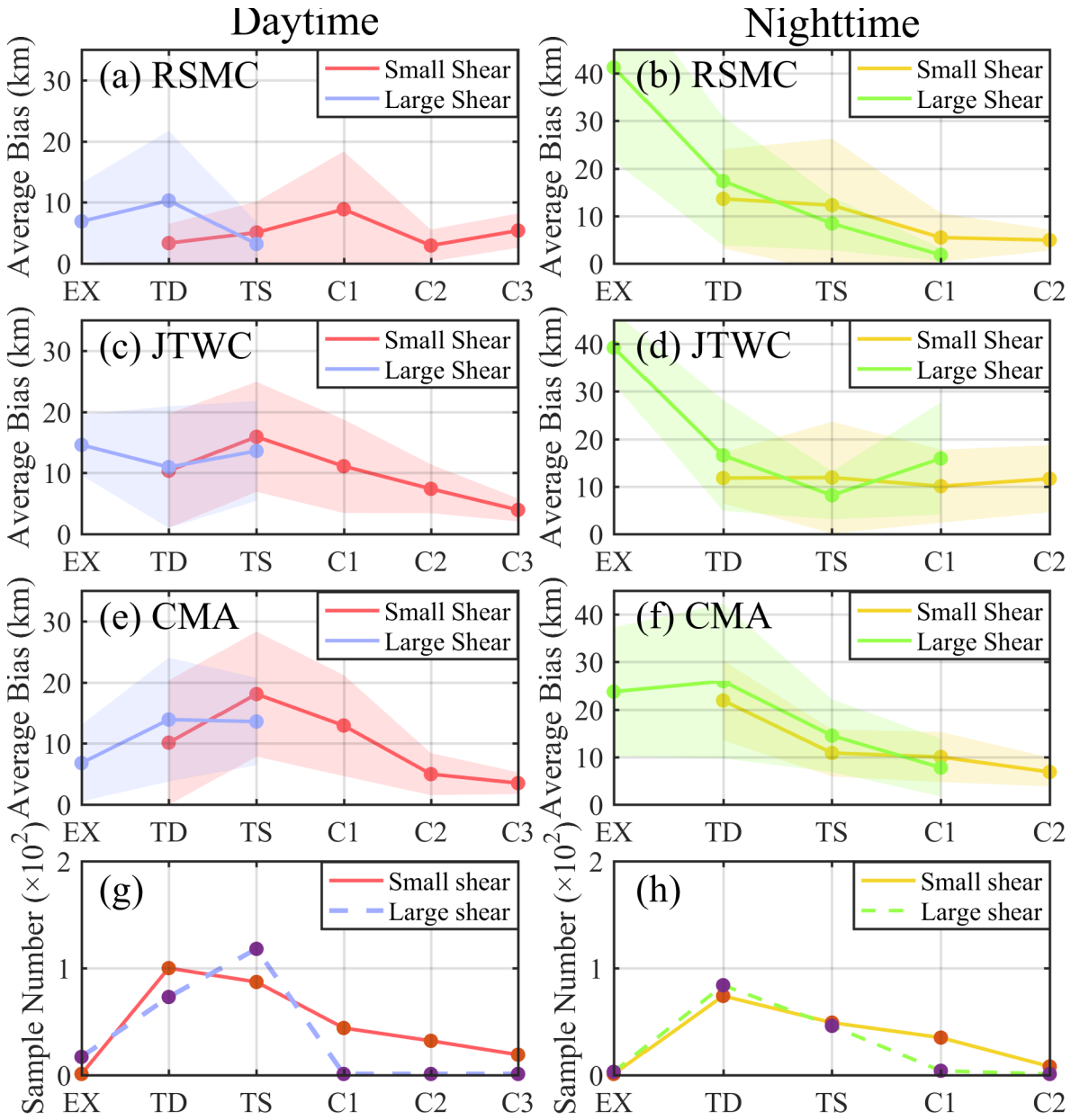


Figure 8. Average biases of the TC center positions between the TC-RGB-based method and the best-track datasets from (**a**,**b**) RSMC-Tokyo, (**c**,**d**) JTWC and (**e**,**f**) CMA-STI, along with (**g**,**h**) sample sizes, for TC cases with exposed LLC centers during 2017–2019 in each intensity category, with shading indicating the standard deviation. Comparisons were conducted for TCs under large/small vertical shear during daytime (left panel) as well as nighttime (right panel).

Figure 9 shows the spatial distribution of the average position biases between the TC-RGB-based method and the three best-track datasets. The position biases of all TC cases on 2° × 2° grid were averaged. In the area of 18° N–36° N over the WNP, the average biases of the three agencies are mostly below 20 km. However, for the area north of 36° N over the WNP, they are mostly above 20 km due to the large vertical wind shear associated with the upper jet at mid-to-high latitudes. In addition, for the area south of 18° N over the WNP, because of the weak TC in the formation stage and the influences of the low-latitude monsoon surge, the average biases are mostly more than 20 km.

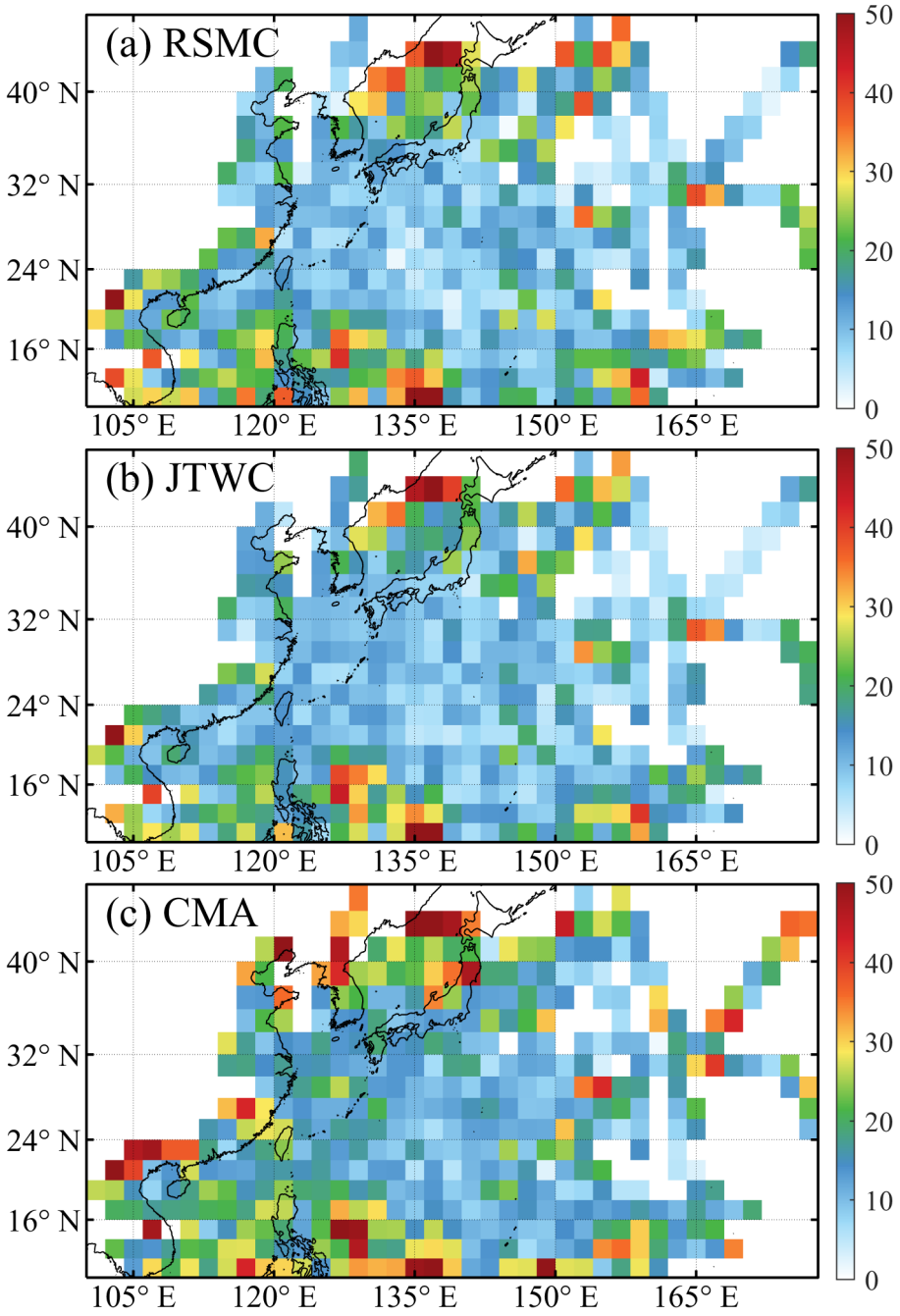


Figure 9. The 2° × 2° gridded distributions of average position biases (unit: km) using 83 TC cases during 2017–2019 between (**a**) RSMC-Tokyo, (**b**) JTWC and (**c**) CMA-STI and the TC-RGB-based method.

4. Discussion

The TC center positions determined by TC-RGB composites need to be verified by using ground truth. The Sentinel-1 SAR measurement, which has been widely used for TC centers, structures and intensity owing to its high spatial resolutions (approximately 1 km), is a choice. However, the sample number of SAR observations is quite small, and most of these samples are focused on the strong TCs with clear eyes that have little controversy in center positions. Although the SAR-based verifications of center positions from the TC-RGB method have been provided in the Appendix A, the results are for reference only.

It is worth noting that the TC center positioning approach based on TC-RGB composites reported in this paper cannot fully represent the true value due to parallax errors of

satellite observations. Specifically, parallax errors are the differences between the satellite observed positions and the apparent positions on the Earth [47]. The two main determinative factors of parallax errors are the satellite viewing angle and the cloud-top height. Under this circumstance, considering most WNP TCs occurring at approximately 130° E of tropical regions, the Himawari-8 with the sub-satellite point at 140.7° E has the smallest parallax errors than other operationally geostationary satellites, such as Chinese Fengyun-4A located at 104.7° E.

In addition, the latitudes and longitudes of the center positions from RSMC-Tokyo, JTWC and CMA-STI are accurate to only one decimal place (0.1° on Earth is approximately 10 km), which means that a center position bias of less than 10 km is also likely to be caused by data accuracy.

5. Conclusions

Multichannel data from AHI were used to produce TC-RGB composites. Under large vertical wind shear, this method can clearly display the exposed LLC, which favors successful TC center positioning. Conversely, in the case of small vertical wind shear, center positioning methods based on TC eye and spiral rain bands are still available for TC-RGB composites.

The characteristics of center position biases between the TC-RGB method and three best-track datasets under different vertical wind shear conditions, intensity categories, and geographical locations were also analyzed. Firstly, via one TC case analysis, it was found that the center position biases of the three agencies were large in a weak TC under large vertical wind shear, which may sometimes exceed 100 km. Secondly, the statistical analysis using 83 WNP TC cases showed that the average center position biases and standard deviations for weak TCs under small vertical wind shear in the daytime are 5 km larger than those under large vertical wind shear at nighttime. Taking 83 TC cases with clear LLC centers into consideration, the difference of these two biases is 10 km. Furthermore, the spatial distribution of the average position biases manifests that biases of more than 20 km were generally located in the areas south of 18° N and north of 36° N over the WNP.

The technique of TC center positioning based on TC-RGB composites could be used in an operational way. However, in the current version this technique is manually handled. Future study will focus on developing an automated routine based on the guideline introduced in Section 2.3.

As an application, the high-accuracy TC center positions from TC-RGB composites shall reveal the small scale features of TC tracks more clearly (e.g., trochoidal motion of the TC eyes). They will also contribute to the improvement of forecast accuracy of TC intensities by variational bogus data assimilation in numerical weather models.

Author Contributions: Conceptualization, X.Z.; methodology, X.Z.; software, L.C.; validation, X.Z.; formal analysis, L.C. and X.Z.; investigation, L.C. and X.Z.; resources, X.Z.; data curation, X.Z.; writing—original draft preparation, L.C. and X.Z.; writing—review and editing, X.Z.; visualization, L.C. and X.Z.; supervision, X.Z., X.T., J.S. and Y.W.; project administration, X.Z.; funding acquisition, X.Z. and X.T. All authors have read and agreed to the published version of the manuscript.

Funding: This research was funded by the National Key Research and Development Programs of China (2017YFC1501603), the National Natural Science Foundation of China (42175006), the Fengyun Application Pioneering Project (FY-APP-2021.0101), and the Basic Research Fund of CAMS (2020R002).

Data Availability Statement: Not applicable.

Acknowledgments: The authors thank Liangxiao Sun, Jian-Feng Gu and three anonymous reviewers for their useful advice on this research. The three TC best-track datasets were provided by JTWC (https://www.metoc.navy.mil/jtwc/jtwc.html?western-pacific, accessed on 10 January 2021), CMA-STI (http://tcdata.typhoon.org.cn/en/zjljsjj_zlhq.html, accessed on 15 January 2021), and RSMC-Tokyo (http://www.jma.go.jp/jma/jma-eng/jma-center/rsmc-hp-pub-eg/besttrack.html, accessed on 26 January 2021), respectively. The FNL data were obtained from the NCEP website (https://rda.ucar.edu/datasets/ds083.3/, accessed on 22 February 2021). The Himawari-8 data used in

our study were downloaded from the website of the Japan Aerospace Exploration Agency (https://www.eorc.jaxa.jp/ptree/, accessed on 22 January 2021) with a registered account.

Conflicts of Interest: The authors declare no conflict of interest.

Appendix A. Preliminary Validation of the TC-RGB-Based Method

Sentinel-1A and -1B were launched by the Copernicus/European Space Agency in 2014 and 2016, respectively. The C-Band SARs onboard Sentinel-1 have both co- and cross-polarization modes. Because ocean backscatters from SAR cross-polarized measurements are quite linear with respect to wind speeds, Sentinel-1 SARs are able to measure sea surface winds up to 150 kt with an acceptable error [48].

TC eye extraction from SAR imagery is an important research topic. Because of the high sensitivity of the measured value by cross-polarization in strong and low wind, the TC eye region is easily distinguished against the eyewall area [49]. At this time, TC centers are set at the geometric center of the eye region. TC centers can also be identified by directly determining the circulation center of the sea surface wind field by wind speed retrievals [49]. It is worth noting that the spatial resolution for the SAR wind field tends to sacrifice to approximately 1 km for high accuracy due to the big noise of the raw product [50].

Sentinel-1 SARs are operated following predefined acquisition plans. Each TC observation requires a specific request submitted through the Copernicus Emergency Management Service two or three days ahead of the acquisition [51]. As a result, valid Sentinel-1 SAR passes over TCs are very sporadic. Only 60 samples (23 TC cases) were collected during 2017–2019 over the WNP basin. They are employed to verify the TC-RGB-based centers. The Sentinel-1 C-Band SAR data were downloaded from CyclObs (https://cyclobs.ifremer.fr/app/, accessed on 29 October 2021).

Figure A1 shows three examples comparing the results of TC center positioning from the TC-RGB composites and the SAR measurements. The first example presents a quasi-circular TC cloud system on a TC-RGB composite image (Figure A1a). However, from SAR measurements, an obvious low-wind center ("eye") is found, and the TC center is positioned at the geometric center of the "eye" (Figure A1b,c). The position bias between the TC-RGB-based center and the SAR-based center is 11 km. The second example presents a TC with an irregularly shaped eye. The rotational center is set as the TC center (Figure A1d). Relative to the SAR-based center (Figure A1e,f), the TC-RGB-based center has a bias of 8 km, which is lower than the best-track data from three agencies. The third example is a TC making landfalls (Figure A1g). Because SAR measurements over land are not valid (Figure A1h,i), the SAR-based center is not believable. The TC-RGB-based center is 77 km away from the SAR-based center. Overall, the position biases between TC-RGB-based centers and SAR-based centers are small before TCs make landfalls.

All of the 60 Sentinel-1 SAR overpasses observing WNP TCs were used to verify the TC center positions determined by the TC-RGB-based method and three best-track datasets. Figure A2 shows the average center position biases, standard deviations and sample sizes of the TC-RGB-based centers and the three best-track datasets under different vertical wind shear. Due to the lack of TC cases at the EX and TD levels, these two levels are not discussed. In Figure A2a, the average biases between the TC-RGB-based centers and the SAR-based centers under large vertical wind shear are smaller than those under small vertical wind shear. Comparing Figure A2a with Figure A2b,d, when the vertical wind shear is large, the TC-RGB-based centers have obviously smaller average center position biases and standard deviations than the RSMC-Tokyo and CMA-STI best-track datasets. This is because the TC-RGB composites can reveal more details about low-level clouds than single-channel images, especially when TCs are under large vertical wind shear. The JTWC dataset has the smallest average center position biases and standard deviations when TCs are at the C2 level, a benefit from the new capabilities of the recent generation of rain-free L-band passive radiometer sensors [33].

It is worth noting that the total sample size of SAR overpasses for WNP TCs during 2017–2019 is quite small, due to the sporadic availability of Sentinel-1 SAR. Moreover,

these samples all focus on TCs in relatively strong intensity categories (above the TS level) without exposed LLC centers, which may not comprehensively show the advantages of the TC-RGB-based method enough. Thus, results presented in this section are for reference only.

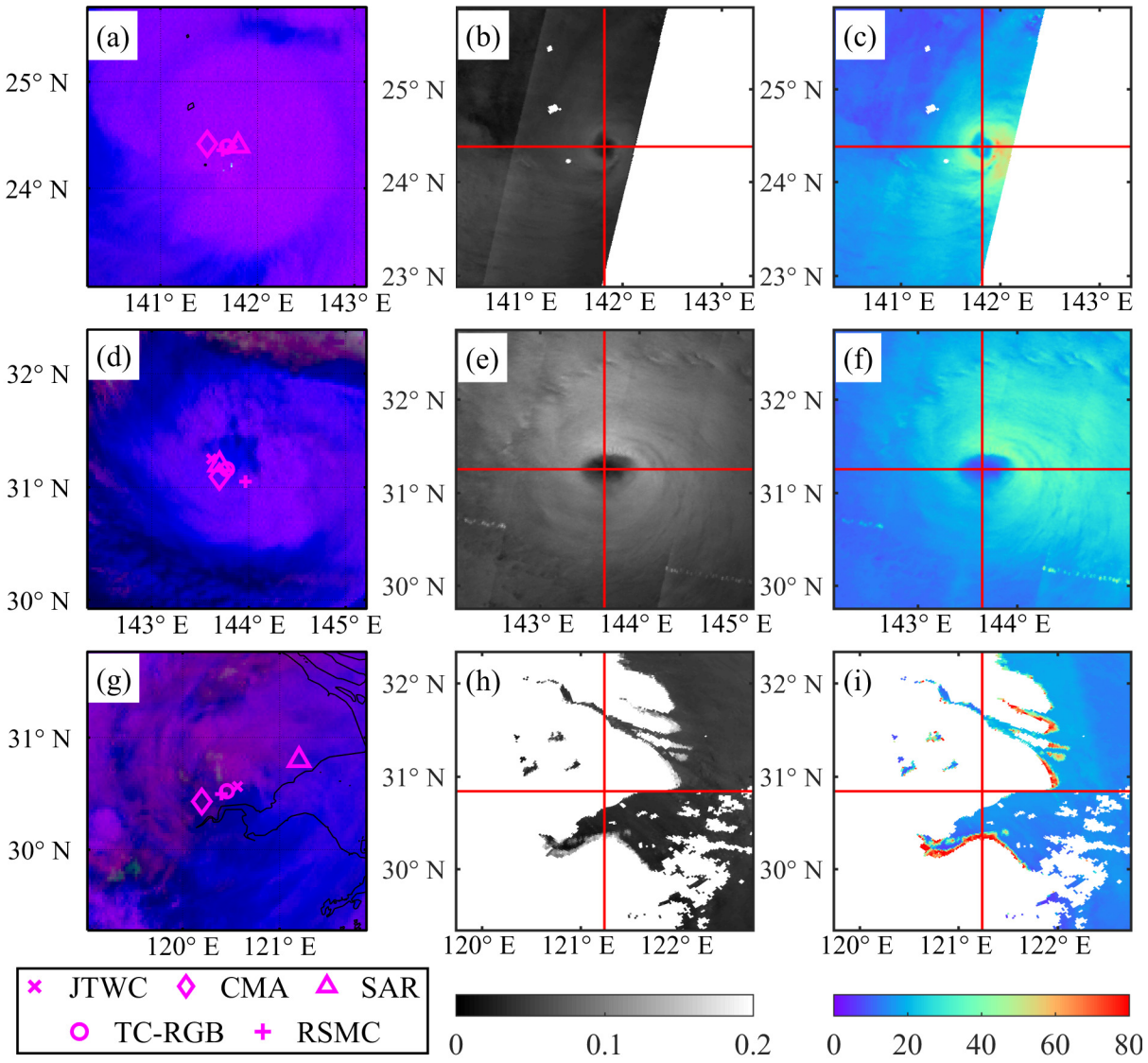


Figure A1. (**a**,**d**,**g**) TC-RGB images, (**b**,**e**,**h**) ocean backscatters from cross-polarized SAR measurements and (**c**,**f**,**i**) SAR sea-surface wind speed retrievals for TC Jongdari (2018) at 2030 UTC on 27 July 2018 (top panel) and 2030 UTC on 26 July 2018 (middle panel) as well as TC Lekima (2019) at 1000 UTC on 10 August 2019 (bottom panel). TC center positions from the three best-track datasets, the TC-RGB-based centers, and the SAR-based centers are indicated by magenta markers.

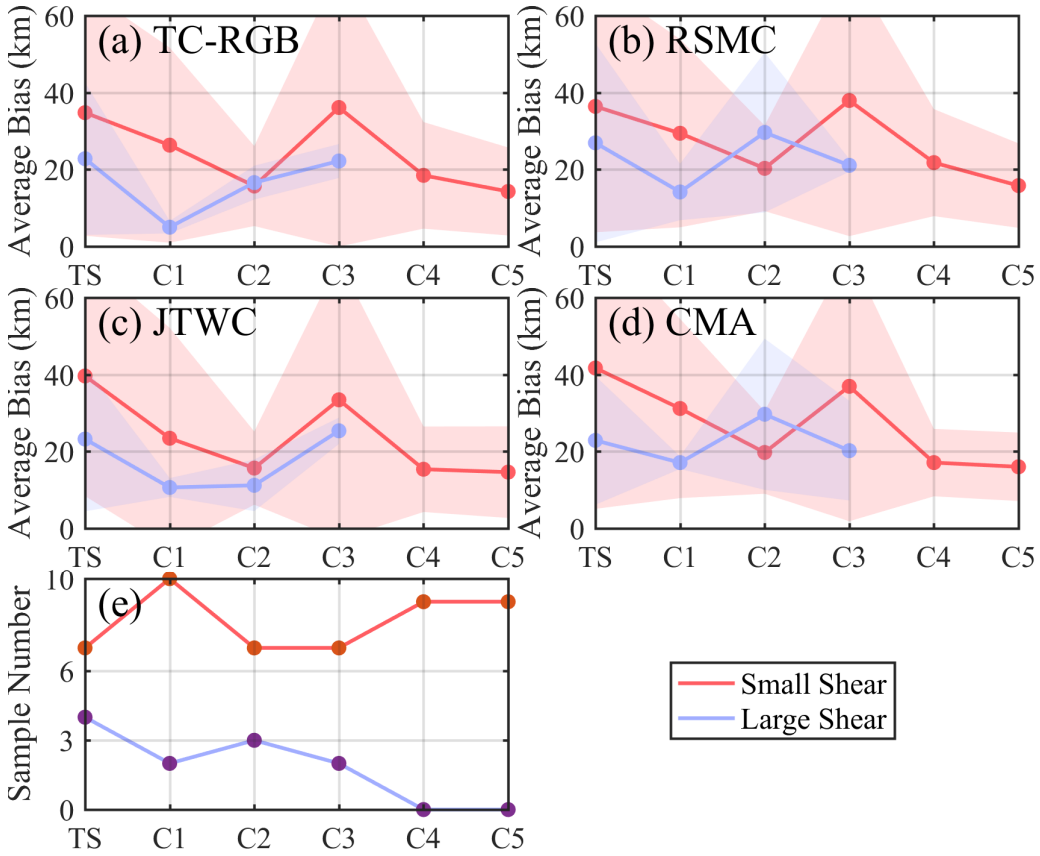


Figure A2. Average biases of the TC center positions between the SAR retrievals and (**a**) TC-RGB-based method or the best-track datasets from (**b**) RSMC-Tokyo, (**c**) JTWC and (**d**) CMA-STI, along with (**e**) sample number, for 60 samples (23 WNP TC cases) during 2017–2019 in each intensity category, with shading indicating the standard deviation.

References

1. Anthes, R.A. Structure and Life Cycle of Tropical Cyclones. In *Tropical Cyclones: Their Evolution, Structure and Effects*, 2nd ed.; American Meteorological Society: Boston, MA, USA, 1982; Volume 19, pp. 11–64.
2. Zhang, Q.; Wu, L.; Liu, Q. Tropical cyclone damages in China 1983–2006. *Bull. Am. Meteorol. Soc.* **2009**, *90*, 489–496. [CrossRef]
3. Peduzzi, P.; Chatenoux, B.; Dao, H.; De Bono, A.; Herold, C.; Kossin, J.; Mouton, F.; Nordbeck, O. Tropical cyclones: Global trends in human exposure, vulnerability and risk. *Nat. Clim. Chang.* **2012**, *2*, 289–294. [CrossRef]
4. Elsberry, R.L. Advances in research and forecasting of tropical cyclones from 1963–2013. *Asia-Pac. J. Atmos. Sci.* **2014**, *50*, 3–16. [CrossRef]
5. Rappaport, E.N.; Franklin, J.L.; Avila, L.A.; Baig, S.R.; Beven, J.L.; Blake, E.S.; Burr, C.A.; Jiing, J.-G.; Juckins, C.A.; Knabb, R.D.; et al. Advances and Challenges at the National Hurricane Center. *Weather Forecast.* **2009**, *24*, 395–419. [CrossRef]
6. Willoughby, H.E.; Chelmow, M.B. Objective determination of hurricane tracks from aircraft observations. *Mon. Weather Rev.* **1982**, *110*, 1298–1305. [CrossRef]
7. Zou, X.; Xiao, Q. Studies on the initialization and simulation of a mature hurricane using a variational bogus data assimilation scheme. *J. Atmos. Sci.* **2000**, *57*, 836–860. [CrossRef]
8. Rozoff, C.M.; Velden, C.S.; Kaplan, J.; Kossin, J.P.; Wimmers, A.J. Improvements in the Probabilistic Prediction of Tropical Cyclone Rapid Intensification with Passive Microwave Observations. *Weather Forecast.* **2015**, *30*, 1016–1038. [CrossRef]
9. Zhuge, X.-Y.; Jian, G.; Yu, F.; Wang, Y. A New Satellite-Based Indicator for Estimation of the Western North Pacific Tropical Cyclone Current Intensity. *IEEE Trans. Geosci. Remote Sens.* **2015**, *53*, 5661–5676. [CrossRef]
10. Zhuge, X.-Y.; Ming, J.; Wang, Y. Reassessing the Use of Inner-Core Hot Towers to Predict Tropical Cyclone Rapid Intensification. *Weather Forecast.* **2015**, *30*, 1265–1279. [CrossRef]
11. Ricchi, A.; Miglietta, M.M.; Bonaldo, D.; Cioni, G.; Rizza, U.; Carniel, S. Multi-Physics Ensemble versus Atmosphere–Ocean Coupled Model Simulations for a Tropical-Like Cyclone in the Mediterranean Sea. *Atmosphere* **2019**, *10*, 202. [CrossRef]
12. Hock, T.F.; Franklin, J.L. The NCAR GPS Dropwindsonde. *Bull. Am. Meteorol. Soc.* **1999**, *80*, 407–420. [CrossRef]
13. Uhlhorn, E.W.; Black, P.G.; Franklin, J.L.; Goodberlet, M.; Carswell, J.; Goldstein, A.S. Hurricane Surface Wind Measurements from an Operational Stepped Frequency Microwave Radiometer. *Mon. Weather Rev.* **2007**, *135*, 3070–3085. [CrossRef]

14. Griffin, J.S.; Burpee, R.W.; Marks Jr, F.D.; Franklin, J.L. Real-time airborne analysis of aircraft data supporting operational hurricane forecasting. *Weather Forecast.* **1992**, *7*, 480–490. [CrossRef]
15. Bell, M.M.; Lee, W.-C. Objective Tropical Cyclone Center Tracking Using Single-Doppler Radar. *J. Appl. Meteorol. Climatol.* **2012**, *51*, 878–896. [CrossRef]
16. Wood, V.T. A technique for detecting a tropical cyclone center using a Doppler radar. *J. Atmos. Ocean. Tech.* **1994**, *11*, 1207–1216. [CrossRef]
17. Velden, C.S.; Olander, T.L.; Zehr, R.M. Development of an objective scheme to estimate tropical cyclone intensity from digital geostationary satellite infrared imagery. *Weather Forecast.* **1998**, *13*, 172–186. [CrossRef]
18. Wimmers, A.J.; Velden, C.S. Objectively Determining the Rotational Center of Tropical Cyclones in Passive Microwave Satellite Imagery. *J. Appl. Meteorol. Climatol.* **2010**, *49*, 2013–2034. [CrossRef]
19. Wimmers, A.J.; Velden, C.S. Advancements in Objective Multisatellite Tropical Cyclone Center Fixing. *J. Appl. Meteorol. Climatol.* **2016**, *55*, 197–212. [CrossRef]
20. Olander, T.L.; Velden, C.S. The Advanced Dvorak Technique: Continued Development of an Objective Scheme to Estimate Tropical Cyclone Intensity Using Geostationary Infrared Satellite Imagery. *Weather Forecast.* **2007**, *22*, 287–298. [CrossRef]
21. Miller, S.; Straka, W.; Mills, S.; Elvidge, C.; Lee, T.; Solbrig, J.; Walther, A.; Heidinger, A.; Weiss, S. Illuminating the Capabilities of the Suomi National Polar-Orbiting Partnership (NPP) Visible Infrared Imaging Radiometer Suite (VIIRS) Day/Night Band. *Remote Sens.* **2013**, *5*, 6717–6766. [CrossRef]
22. Meissner, T.; Wentz, F.J.; Ricciardulli, L. The emission and scattering of L-band microwave radiation from rough ocean surfaces and wind speed measurements from the Aquarius sensor. *J. Geophys. Res. Ocean.* **2014**, *119*, 6499–6522. [CrossRef]
23. Mayers, D.; Ruf, C. Tropical Cyclone Center Fix Using CYGNSS Winds. *J. Appl. Meteorol. Climatol.* **2019**, *58*, 1993–2003. [CrossRef]
24. Mayers, D.; Ruf, C. MTrack: Improved Center Fix of Tropical Cyclones from SMAP Wind Observations. *Bull. Am. Meteorol. Soc.* **2021**, *102*, E700–E709. [CrossRef]
25. Lee, T.E.; Miller, S.D.; Turk, F.J.; Schueler, C.; Julian, R.; Deyo, S.; Dills, P.; Wang, S. The NPOESS VIIRS day/night visible sensor. *Bull. Am. Meteorol. Soc.* **2006**, *87*, 191–200. [CrossRef]
26. Zhang, G.; Perrie, W.; Li, X.; Zhang, J.A. A Hurricane Morphology and Sea Surface Wind Vector Estimation Model Based on C-Band Cross-Polarization SAR Imagery. *IEEE Trans. Geosci. Remote Sens.* **2017**, *55*, 1743–1751. [CrossRef]
27. Miller, S.D.; Mills, S.P.; Elvidge, C.D.; Lindsey, D.T.; Lee, T.F.; Hawkins, J.D. Suomi satellite brings to light a unique frontier of nighttime environmental sensing capabilities. *Proc. Natl. Acad. Sci. USA* **2012**, *109*, 15706–15711. [CrossRef]
28. Miller, S.D.; Straka, W.C.; Yue, J.; Seaman, C.J.; Xu, S.; Elvidge, C.D.; Hoffmann, L.; Azeem, I. The Dark Side of Hurricane Matthew: Unique Perspectives from the VIIRS Day/Night Band. *Bull. Am. Meteorol. Soc.* **2018**, *99*, 2561–2574. [CrossRef]
29. Schueler, C.F.; Clement, J.E.; Ardanuy, P.E.; Welsch, C.; DeLuccia, F.; Swenson, H. NPOESS VIIRS Sensor Design Overview. In Proceedings of the Earth Observing Systems VI, San Diego, CA, USA, 1–3 August 2001; pp. 11–23.
30. Lensky, I.; Rosenfeld, D. Clouds-aerosols-precipitation satellite analysis tool (CAPSAT). *Atmos. Chem. Phys.* **2008**, *8*, 6739–6753. [CrossRef]
31. Hawkins, J.D.; Solbrig, J.E.; Miller, S.D.; Surratt, M.; Lee, T.F.; Bankert, R.L.; Richardson, K. Tropical Cyclone Characterization via Nocturnal Low-Light Visible Illumination. *Bull. Am. Meteorol. Soc.* **2017**, *98*, 2351–2365. [CrossRef]
32. Song, J.-J.; Wang, Y.; Wu, L. Trend discrepancies among three best track data sets of western North Pacific tropical cyclones. *J. Geophys. Res.* **2010**, *115*, D12128. [CrossRef]
33. JTWC. Annual Tropical Cyclone Report 2017. 2017. Available online: http://www.metoc.navy.mil/jtwc/products/atcr/2017atcr.pdf (accessed on 16 March 2021).
34. Simpson, R.H.; Saffir, H. The hurricane disaster potential scale. *Weatherwise* **1974**, *27*, 169. [CrossRef]
35. Kalnay, E.; Kanamitsu, M.; Kistler, R.; Collins, W.; Deaven, D.; Gandin, L.; Iredell, M.; Saha, S.; White, G.; Woollen, J. The NCEP/NCAR 40-year reanalysis project. *Bull. Am. Meteorol. Soc.* **1996**, *77*, 437–472. [CrossRef]
36. DeMaria, M.; Mainelli, M.; Shay, L.K.; Knaff, J.A.; Kaplan, J. Further improvements to the statistical hurricane intensity prediction scheme (SHIPS). *Weather Forecast.* **2005**, *20*, 531–543. [CrossRef]
37. Bessho, K.; Date, K.; Hayashi, M.; Ikeda, A.; Imai, T.; Inoue, H.; Kumagai, Y.; Miyakawa, T.; Murata, H.; Ohno, T.; et al. An Introduction to Himawari-8/9—Japan's New-Generation Geostationary Meteorological Satellites. *J. Meteorol. Soc. Jpn. Ser. II* **2016**, *94*, 151–183. [CrossRef]
38. Zhuge, X.; Zou, X.; Wang, Y. Determining AHI Cloud-Top Phase and Intercomparisons with MODIS Products Over North Pacific. *IEEE Trans. Geosci. Remote Sens.* **2021**, *59*, 436–448. [CrossRef]
39. Zhuge, X.; Zou, X.; Wang, Y. AHI-Derived Daytime Cloud Optical/Microphysical Properties and Their Evaluations with the Collection-6.1 MOD06 Product. *IEEE Trans. Geosci. Remote Sens.* **2021**, *59*, 6431–6450. [CrossRef]
40. Tomasi, C.; Petkov, B.; Mazzola, M.; Ritter, C.; di Sarra, A.; di Iorio, T.; del Guasta, M. Seasonal Variations of the Relative Optical Air Mass Function for Background Aerosol and Thin Cirrus Clouds at Arctic and Antarctic Sites. *Remote Sens.* **2015**, *7*, 7157–7180. [CrossRef]
41. Inoue, T. A cloud type classification with NOAA 7 split-window measurements. *J. Geophys. Res. Atmos.* **1987**, *92*, 3991–4000. [CrossRef]
42. Ellrod, G.P. Advances in the detection and analysis of fog at night using GOES multispectral infrared imagery. *Weather Forecast.* **1995**, *10*, 606–619. [CrossRef]

43. Yamanouchi, T.; Kawaguchi, S. Cloud distribution in the Antarctic from AVHRR data and radiation measurements at the surface. *Int. J. Remote Sens.* **1992**, *13*, 111–127. [CrossRef]
44. Dvorak, V.F. Tropical Cyclone Intensity Analysis and Forecasting from Satellite Imagery. *Mon. Weather Rev.* **1975**, *103*, 420–430. [CrossRef]
45. Willoughby, H.E. A Possible Mechanism for the Formation of Hurricane Rainbands. *J. Atmos. Sci.* **1978**, *35*, 838–848. [CrossRef]
46. Lu, X.; Yu, H.; Yang, X.; Li, X.; Tang, J. A new technique for automatically locating the center of tropical cyclones with multi-band cloud imagery. *Front. Earth Sci.* **2019**, *13*, 836–847. [CrossRef]
47. Vicente, G.A.; Davenport, J.C.; Scofield, R.A. The role of orographic and parallax corrections on real time high resolution satellite rainfall rate distribution. *Int. J. Remote Sens.* **2010**, *23*, 221–230. [CrossRef]
48. Mouche, A.; Chapron, B.; Knaff, J.; Zhao, Y.; Zhang, B.; Combot, C. Copolarized and Cross-Polarized SAR Measurements for High-Resolution Description of Major Hurricane Wind Structures: Application to Irma Category 5 Hurricane. *J. Geophys. Res. Ocean.* **2019**, *124*, 3905–3922. [CrossRef]
49. Guosheng, Z.; Biao, Z.; Perrie, W.; Qing, X.; Yijun, H. A Hurricane Tangential Wind Profile Estimation Method for C-Band Cross-Polarization SAR. *IEEE Trans. Geosci. Remote Sens.* **2014**, *52*, 7186–7194. [CrossRef]
50. Mouche, A.A.; Chapron, B.; Zhang, B.; Husson, R. Combined Co- and Cross-Polarized SAR Measurements Under Extreme Wind Conditions. *IEEE Trans. Geosci. Remote Sens.* **2017**, *55*, 6746–6755. [CrossRef]
51. Knaff, J.A.; Sampson, C.R.; Kucas, M.E.; Slocum, C.J.; Brennan, M.J.; Meissner, T.; Ricciardulli, L.; Mouche, A.; Reul, N.; Morris, M.; et al. Estimating tropical cyclone surface winds: Current status, emerging technologies, historical evolution, and a look to the future. *Trop. Cyclone Res. Rev.* **2021**, *10*, 125–150. [CrossRef]